

Dispersion characteristics for plasma resonances of Maxwellian and Kappa distribution plasmas and their comparisons to the IMAGE/RPI observations

Adolfo F.-Viñas⁽¹⁾, Richard L. Mace⁽²⁾ and Robert F. Benson⁽¹⁾

⁽¹⁾ Laboratory for Extraterrestrial Physics, NASA-Goddard Space Flight Center,
Greenbelt, MD 20771, U.S.A.

⁽²⁾ Department of Physics, University of KwaZulu-Natal, Pietermaritzburg, South Africa

Abstract

The Radio Plasma Imager (RPI) on the IMAGE satellite stimulates short-range plasma wave echoes and plasma emissions, known as plasma resonances, which are then displayed on plasmagrams. These resonances are used to provide measurements of the local electron density n_e and magnetic field strength $|\mathbf{B}|$. The RPI-stimulated resonances are the magnetospheric analog of plasma resonances stimulated by topside ionospheric sounders. These resonances are stimulated at the harmonic of the electron cyclotron frequency f_{ce} , the electron plasma frequency f_{pe} , and the upper-hybrid frequency f_{uh} (where $f_{uh}^2 = f_{pe}^2 + f_{ce}^2$). They are also observed between the harmonics of f_{ce} (i.e., nf_{ce}) both above and below f_{pe} , where they are known as Qn and Dn resonances, respectively. Calculations of the Qn resonances in the ionospheric environment, based upon a thermal Maxwellian plasma model provided confidence in the resonance identification between the observations and the estimated values within the experimental errors. However, there is often an apparent difference between these resonances in the magnetospheric environment and those predicted by calculations based on a Maxwellian plasma model. For example, the Qn's are often (and perhaps consistently) observed at frequencies slightly lower than expected for a Maxwellian plasma. We present a new set of resonance calculations using the dispersion characteristics of these resonances based upon a non-thermal kappa distribution. We then compare these calculations, and those based on a traditional Maxwellian thermal plasma model, with the IMAGE/RPI observations. The calculations based on the kappa distribution model appear to resolve the aforementioned frequency discrepancy. In addition, the results also provide insights into the nature of the electron distribution function in the magnetosphere.

1. Introduction.

Natural banded emissions are frequently observed by spacecraft in low inclination orbits in the terrestrial magnetosphere (for a review see Kennel and Ashour-Abdalla, [1982]) and in the magnetospheres of other planets, e.g., Jupiter, Saturn and Uranus where in-situ measurements have been obtained [Kurth, 1992]. The most important feature of these emissions, which is common to all these observations, is that they occur between harmonics of the electron cyclotron frequency. Several interpretations of these emissions of magnetospheric origin have related them to plasma resonances stimulated by ionospheric topside sounders because of the similarity in the observed frequency spectra [Fredricks, 1971; Oya, 1972; Christiansen et al., 1978; Benson and Osherovich, 1992; Osherovich et al., 1993; Benson et al., 2001]. These resonances are observed both above and below the electron plasma frequency f_{pe} , and are known as Qn and Dn resonances, respectively. In addition to these resonances, the ionospheric topside sounders also produce plasma resonances at the harmonics of the electron cyclotron frequency f_{ce} , f_{pe} , and the upper-hybrid frequency f_{uh} , where $f_{uh}^2 = f_{pe}^2 + f_{ce}^2$ [see, e.g., the review by Muldrew, 1972a]. They have also been stimulated and induced in the magnetosphere by the Radio Plasma Imager (RPI) on the IMAGE satellite [Benson et al., 2003]. These resonances provide an independent diagnostic method for determining the local electron density n_e and magnetic field strength $|\mathbf{B}|$ and can be used as an inversion tool to infer properties of the plasma particle distribution function.

It is generally well known that the dispersion characteristics ($\omega - k$ diagram) of the Bernstein modes (at least for Maxwellian distributions) change considerably between harmonics of the cyclotron frequency when one compares the dispersion curves of the cyclotron band that contains the upper hybrid waves, and the bands above it, with those bands below the one containing the upper hybrid frequency. In other words, a Bernstein mode propagates in each cyclotron harmonic band $n\Omega_e < \omega < (n+1)\Omega_e$, but how it does so depends upon whether their frequency lies above, below, or in the upper hybrid frequency band. The waves in those bands with $\omega < \omega_{uh}$ start at frequencies $\omega \approx (n+1)\Omega_e$ at long wavelengths (i.e. small $\lambda_e = k_{\perp}^2 \rho_e^2 / 2$) and descend to $\omega \approx n\Omega_e$ when $\lambda_e \gg n$. Those waves with $\omega > \omega_{uh}$ start at $\omega \approx n\Omega_e$ ascend to a peak near $\lambda_e \propto n$, or similarly $k_{\perp} \rho_e \propto \sqrt{2n}$, and then return to $\omega \approx n\Omega_e$ for $\lambda_e \gg n$ [Kamimura, et. al., 1978]. In these high frequency harmonic bands, the modes have a zero group velocity ($v_g = \partial\omega / \partial k = 0$) for $\lambda_e \propto n$, and therefore there is a neighboring range of λ_e for which the group velocity is small. Thus the bands at the upper hybrid level and above are limited to only part of the frequency range, whereas those below the upper hybrid branch extend over the entire range of frequencies between the harmonics. These peaks in the dispersion profiles, known as the Qn-resonances, do not exist for the cyclotron bands below the upper hybrid level. They only appear in the high frequency electrostatic regime (i.e., the short wavelengths regime where $|k_{\perp} \rho_e| \approx O(1)$ or greater) of the dispersion profile suggesting that they are of electrostatic nature. The Qn resonances, as generated by ionospheric topside sounders, have been attributed to a close matching of the perpendicular group velocity v_g of the propagating Bernstein (or ECH) waves to the satellite velocity v_s [Muldrew, 1972]. The wave in the upper hybrid branch is special since the electrostatic band starts at $\omega = \omega_{uh}$, rather than at the next higher cyclotron harmonic, and

then descends to the next lower cyclotron harmonic frequency as λ_e increases after reaching a peak frequency.

The RPI on the IMAGE satellite stimulates short-range electrostatics echoes and long-range electromagnetic echoes in the Earth's magnetosphere. The resultant data are presented in either a conventional frequency versus time spectrogram (passive mode) or in plasmagrams (active mode) that display the amplitude of the received echo and its virtual range (i.e., assuming free-space speed of light propagation) as a function of sounding frequency (see Reinish et al. [2000] for a description of the instrument and data formats). These plasmagrams are the magnetospheric analog of topside-sounders ionograms [Benson et al., 2003]. In this work we will concern ourselves mainly with the electrostatic echoes, i.e., the signals known as plasma resonances because of their spike-like appearance on the plasmagrams. They correspond to waves of slow group velocity that return to the spacecraft following the short-duration RPI pulse. The cutoff frequency of an electromagnetic echo provides additional confidence in the determination of the local electron density.

The observation of these Qn resonances in the ionosphere provided confidence in the resonance identification and consequently their use as an independent diagnostic method for determining the local electron density n_e and magnetic field strength $|\mathbf{B}|$. Recent RPI measurements in the magnetosphere, however, often show a definite difference between the observed resonance values and those values estimated from theoretical calculations of the dispersion properties of Bernstein waves for an isotropic Maxwellian plasma. In these cases, the Qn's are observed at frequencies consistently lower (within the experimental errors) than expected for a Maxwellian plasma, suggesting a departure from such distributions. Christiansen et. al. [1971] suggested that the identification of the frequencies of natural emissions, that appear to be related to the Qn frequencies, can be explained in terms of a non-thermal plasma that contains a tail population of suprathermal particles. In an attempt to explain, on theoretical grounds, such non-thermal conditions Belmont [1981] suggested that the dispersion characteristics of these resonances not only depends on the density or magnetic field strength, but also on the shape of the distribution function (which has been generally assumed to be Maxwellian). The idea that the wave dispersion characteristics are not only dependent on the physical parameters (e.g., density, temperature, magnetic field, etc.), but that they also depend on the shape of the distribution was first postulated by Abraham-Shrauner and Feldman [1977a,b] in application to whistler and electromagnetic ion cyclotron waves in the solar wind. Belmont [1981] numerically calculated the dispersion characteristics for two model distribution functions: a) a background finite temperature Maxwellian plasma mixed with a ring distribution of low density and zero temperature (e.g., a delta function in the transverse direction relative to the background magnetic field), and b) the superposition of two finite temperature Maxwellians, one cold and the other hot. The results of their calculations indicated that the second model (case b) was more consistent with the resonance observations. This model, although very reasonable, requires the variation of at least four parameters (two densities and two temperatures) in order for the model to reproduce the variations in the shape of the distribution function and explain the frequency dispersion characteristic of the Bernstein waves. In general this model has a small effect on the dispersion characteristics, since it remains fundamentally Maxwellian (but with more parameters) and the dielectric tensor becomes just the sum of the dielectric tensors for each Maxwellian component; therefore no fundamental change in the dielectric tensor occurs.

The purpose of this work is to present a new set of resonance dispersion characteristic calculations based upon an isotropic non-thermal kappa distribution function and to compare these calculations, and those obtained from an isotropic Maxwellian thermal plasma, with IMAGE/RPI observations. The goal is not only to provide an independent diagnostic method for determining the local electron density n_e and magnetic field strength $|\mathbf{B}|$, but to establish a diagnostic inversion tool to provide insights into the nature of the electron velocity distribution function in the magnetosphere. The model requires only three parameters to define the shape and characteristics of the distribution function. The kappa distribution fundamentally changes the form of the dielectric tensor [Mace, 1996; Mace, 2004]. Each tensor element now depends additionally on κ , the spectral index of the velocity distribution, which controls the shape of its profile. Varying κ from $\kappa > 3/2$ to infinity permits the study of a wide variety of different plasma conditions, ranging at the extremes, from highly accelerated tails to the thermal Maxwellian case, without changing the model equations.

2. The distribution function and theoretical linear dispersion relation model.

In this section we present a kappa velocity distribution function model. Kappa distributions are similar to the velocity distributions predicted by Tsallis [1988, 2004] and Tsallis and Brigatti [2004] from an entropy principle based upon non-extensive statistical mechanics. Tsallis generalized the traditional Boltzmann-Gibbs-Shannon entropy to understand physical non-equilibrium systems (or systems having strong non-Markovian microscopic memory and multifractal structured systems) where long-range interactions or long-memory effects are important, such as those in space plasmas. These aspects have been recently emphasized by Leubner [2004], who showed a link between the kappa distribution and the Tsallis distribution where κ measures the degree of non-extensivity of the system. One recovers the extensivity (additivity) as $\kappa \rightarrow \infty$ where the system is described by a Maxwellian velocity distribution. The Tsallis formalism provides a potentially important microscopic foundation that justifies the theory of the kappa velocity distribution.

We also considered a theoretical dispersion relation for electromagnetic Bernstein wave modes based upon the kappa velocity distribution. Here we consider a non-relativistic plasma system composed of electrons and ions, but where the ion dynamical response is neglected since the frequency of the waves we are considering are much greater than any characteristic frequency associated with the ions. Thus, the ions are treated as a homogeneous neutralizing background plasma where $M_p \gg m_e$. We further assume that the electron plasma is isotropic (i.e., $T_e = T_{\perp e} = T_{\parallel e}$), has no drift, and is characterized by a kappa velocity distribution function. The kappa velocity distribution resembles a Maxwellian distribution at low velocities while at suprathermal velocities it reduces to a power law. It is defined as follows [Summers and Thorne, 1991]

$$f_e(v) = \frac{A_\kappa}{\left(1 + \frac{v^2}{\kappa \theta_e^2}\right)^{\kappa+1}} \quad \text{where} \quad A_\kappa = n_e \left(\pi \kappa \theta_e^2\right)^{-3/2} \frac{\Gamma(\kappa+1)}{\Gamma(\kappa-1/2)} \quad \text{for} \quad \kappa > 3/2 \quad (1)$$

where $\theta_e^2 = 2((\kappa - 3/2)/\kappa)\alpha_e^2$ and $\alpha_e^2 = (T_e/m_e)$. This distribution reduces to an ordinary Maxwellian with a thermal speed α_e in the limit $\kappa \rightarrow +\infty$. A further inspection of the kappa distribution shows that it only depends on three parameters, i.e., an electron density n_e , an electron temperature T_e and κ (i.e., the spectral index of the kappa distribution) that controls the shape of the distribution function. Figure 1 shows the profile of the kappa distribution function for different values of κ (i.e., $\kappa = 2, 3, 5$) including a Maxwellian distribution (i.e., $\kappa = +\infty$) in arbitrary normalized units. The most important aspect of this figure is that the shape of the distribution function is controlled by the spectral index κ . Note that the number of suprathermal particles increases as κ decreases from a Maxwellian distribution model.

Recent calculations by Mace [2003, 2004] based upon a Gordeyev integral approach provided general expressions for the dispersion relation of both electrostatic and electromagnetic Bernstein-mode waves, which propagate perpendicular to the background magnetic field in a uniform, isotropic, non-relativistic plasma, that is described by a kappa distribution. Because the calculations for the derivation of the dispersion relation are tedious and extensive, we will not duplicate them here, but will only present the form of the electrostatic expression. The form of the dispersion relation for the electromagnetic case is presented in Appendix A. The electrostatic dispersion relation $\Lambda_\kappa^{es}(\omega, k, \theta = 90) = 0$ for perpendicular-propagating Bernstein waves in a kappa distribution plasma is given by [Mace, 2003, 2004]

$$\Lambda_\kappa^{es}(\omega, k, \theta = 90) = 1 + \sum_s \frac{1}{k^2 \lambda_{\kappa,s}^2} \left\{ R_s \left(\kappa, \frac{\omega}{\Omega_s}, 2\lambda_s' \right) + \pi^{1/2} \frac{\omega}{\Omega_s} \csc \left(\pi \frac{\omega}{\Omega_s} \right) S_s \left(\kappa, \frac{\omega}{\Omega_s}, 2\lambda_s' \right) \right\} = 0$$

$$R_s \left(\kappa, \frac{\omega}{\Omega_s}, 2\lambda_s' \right) = 1 - {}_2F_3 \left[1, \frac{1}{2}; \frac{1}{2} - \kappa, 1 + \frac{\omega}{\Omega_s}, 1 - \frac{\omega}{\Omega_s}; 2\lambda_s' \right]$$

$$S_s \left(\kappa, \frac{\omega}{\Omega_s}, 2\lambda_s' \right) = \frac{(2\lambda_s')^{\kappa+1/2} \Gamma(\kappa+1) \Gamma(1/2-\kappa)}{\Gamma(\kappa+3/2+\omega/\Omega_s) \Gamma(\kappa+3/2-\omega/\Omega_s)} {}_1F_2 \left[\kappa+1; \kappa+\frac{3}{2}+\frac{\omega}{\Omega_s}, \kappa+\frac{3}{2}-\frac{\omega}{\Omega_s}; 2\lambda_s' \right]$$

where the subscript s represent the particle specie ($s = e$ for electrons and $s = i$ for ions), ω is the wave frequency, $k = k_\perp$ is the perpendicular wave vector, θ is the propagation angle restricted only to perpendicular propagation with relation to the background magnetic field \mathbf{B} , ω_{ps} and Ω_s are the plasma and cyclotron frequencies, respectively. In the above expression we also defined the Debye length ($\lambda_{\kappa,s}$) for a kappa plasma and the square of the normalized wavevector (λ_s') (correcting a typographical error in Mace [2004]) as

$$\lambda_{\kappa,s} = \left[\frac{(\kappa - 3/2)}{(\kappa - 1/2)} \frac{\alpha_s^2}{\omega_{ps}^2} \right]^{1/2} \quad \text{and} \quad \lambda_s' = (\kappa - 3/2) k^2 \alpha_s^2 / \Omega_s^2, \quad (3)$$

which are defined in terms of the thermal speed α_s or gyroradius ρ_s and also depend on the electron density n_e , the electron temperature T_e , and the magnetic field strength B . Here, the functions ${}_1F_2$ and ${}_2F_3$ are the generalized hypergeometric functions. In general the shape parameter κ is different for each specie (i.e., $\kappa = \kappa_s$). For this work however, since the only dynamical specie are the electrons, we will assume that κ is a constant for that specie.

The electromagnetic dispersion relation $\Lambda_\kappa^{em}(\omega, k, \theta = 90) = 0$ for Bernstein modes [Mace, 2004] also depends on similar parameters, so we refer to it by a similar notation

$$\Lambda_\kappa^{em}(\omega, k, \theta = 90; \omega_{ps}/\Omega_s, \lambda'_s) = 0 \quad (4)$$

but the details of the expression are left for Appendix A. We also present in the Appendix, the electrostatic and electromagnetic dispersion relation for a Maxwellian plasma (i.e., when $\kappa \rightarrow +\infty$). The Maxwellian dispersion relation is presented in a manner similar to that given by Stix [1992], Oya [1971] and Puri et al. [1973]

The expressions above seem considerably complex, however they can be solved numerically with great accuracy. Figure 2 is an example of the numerical solution of the electromagnetic dispersion relation for kappa (see equation A.2) and Maxwellian distributions (see equation A.7) for Bernstein mode waves in the case of an electron plasma with a temperature of about 51eV (i.e., $\alpha_e/c = 0.01$ where c is the vacuum speed of light), a ratio of the upper hybrid frequency to cyclotron frequency of $\omega_{uh}/\Omega_e = 4.5$ (i.e., $\omega_{pe}/\Omega_e = 4.39$), and $\kappa = 2$. It shows the wave frequency ω/Ω_e versus wave vector $k\rho_e$ in normalized dimensionless units for different bands of the Bernstein modes. Figure 2 shows that the Bernstein modes for a kappa plasma can support the previously discussed Qn waves, depending on whether the mode's frequency at vanishing $k\rho_e$ lies above or below the upper hybrid frequency $\omega_{uh}/\Omega_e = 4.5$. A comparison of the solutions for the kappa and Maxwellian distributions illustrate that, irrespective of the frequency domain, there are considerable differences in the dispersion relation, suggesting a significant dependence of the shape of the distribution function. This was also clearly illustrated by Mace [2004] who considered several values of κ . Furthermore, note that the solution of the dispersion relation illustrated in Figure 2 covers the full range of domain of the electromagnetic Bernstein waves for which $|k\rho_e| \ll 1$ to the electrostatic regimes for which $|k\rho_e| \geq 1$. Thus, for completeness, we also present the dispersion relation for the electromagnetic extraordinary (X) mode as determined from the dispersion relation for kappa and Maxwellian distributions. Note that these solutions are superposed on each other indicating that they are identical and suggesting that for perpendicular propagating electromagnetic waves there is basically no difference between the two velocity distributions in the electromagnetic domain. Nevertheless, this is not the case for the electrostatic regime in which significant differences between the dispersion relations are observed.

In the next section we compare the numerical solution of both the dispersion relation for kappa and Maxwellian distributions of Bernstein waves with observed resonances from the IMAGE/RPI instrument.

3. The IMAGE/RPI observations

Figure 3 shows RPI data in the form of a plasmagram obtained when IMAGE was at a geocentric distance of about $6.0 R_E$ as it approached apogee. The plasmagram shows Qn resonances with $n = 5$ to 9 in the observed frequency range. During this time, other resonances were identified, and an electromagnetic X-mode echo trace, that enabled the plasma conditions appropriate for this record to be determined [Benson et al., 2003]. From the nf_{ce} resonances (observed from $n = 2$ to 9) an average value for $f_{ce} = 4.73 \pm 0.02$ kHz was determined. Using this value, and the observed resonances at f_{pe} and f_{uh} , a self-consistent value for $f_{pe} = 26.4 \pm 0.2$ kHz was obtained that yielded an X-mode cutoff frequency consistent with a projection of the observed portion of the reflection trace to zero virtual range. Thus for this record, $f_{pe}/f_{ce} = 5.58 \pm 0.07$ and $f_{uh}/f_{ce} = 5.67 \pm 0.07$. Note that the nf_{ce} resonances appear without Qn resonances when $nf_{ce} < f_{pe}$ and that the Qn resonances observed when $nf_{ce} > f_{uh}$ tend to merge with the nf_{ce} resonances as n increases. Also note that there are more short time delay (i.e., low virtual range) sounder-stimulated emissions between the nf_{ce} values in the frequency domain below f_{pe} than above it. These emissions are attributed to the Dn resonances [Benson et al., 2003]. There are also strong natural emissions, i.e., signals of equal intensity in all virtual range bins, between the nf_{ce} values (particularly in the frequency domain below f_{pe}). Figure 4 presents an enlargement of Figure 3 in the frequency range of interest for the present investigation, i.e., the region containing the Qn resonances, for all three receiving antennas. Since the received signals are the result of propagation paths from the transmitting X antenna, an inspection of the data from all three receiving antennas leads to the best determination of the Qn frequencies. These records clearly illustrate the wide effective bandwidth of strong sounder-stimulated magnetospheric resonances (typically 5 to 6 times the RPI receiver bandwidth) [Benson et al., 2003]. The normalized values for the Qn resonances observed in Figures 3 and 4 are presented in Table 1.

In order to fit the resonances, we used the observed ratio of f_{uh}/f_{ce} (or f_{pe}/f_{ce}). Since the solution of the dispersion relation in the electrostatic regime is highly insensitive to the temperature (it is more sensitive to the temperature anisotropy; however this is not the situation considered in this work) we fix the value of the temperature to about 51 eV, which is a reasonable value for the inner magnetosphere. The solutions over the frequency and wave number ranges considered, however, are identical to those we would have obtained had we used a value of 1 keV for the temperature, which is typical of tail outer magnetosphere conditions. In order to obtain the value of κ , we required that all the Qn-resonances are generated in the same plasma region, characterized by a single value of κ . In other words, we treat the resonances as in the field of spectrography, where the spectral lines are produced by similar plasma characteristics. Thus, by a trial and error bracketing scheme we seek to find the κ value that best fits the lowest and highest Qn-resonances within the measured error bounds, and then we proceed with such value to obtain the frequency characteristics of all the intermediate Qn-resonances. This scheme seems the most reasonable and provides the most confidence in the solution.

Figure 5 present the dispersion characteristics of the Bernstein mode waves with $\omega \geq \omega_{uh}$ obtained from the numerical solution of the dispersion relation for a Maxwellian and kappa distributions for the parameters corresponding to the April 8, 2002 RPI data of Figures 3 and 4. The bracketing search yields $\kappa = 2.1$ as the best value that fits the lowest and highest (i.e., $n = 5$ and 9 respectively) Qn resonances, so we fix this value for the solution of all other intermediate

resonances of the dispersion curves. Thus, Figure 5 shows the normalized frequency (ω/Ω_{ce}) as a function of the normalized perpendicular wave vector ($k\rho_e$) over two orders of magnitude for the Qn bands between 5 to 9 in the electrostatic regime (i.e., $0.1 < k\rho_e < 10$). Dispersion calculations were only performed for those bands corresponding to conditions for the Qn resonances, i.e., for the bands containing the ω_{uh} and for those at higher frequencies. Note that the maximum frequency peak of the Qn resonances for the kappa velocity distribution, lie consistently below those value obtained from a Maxwellian velocity distribution. These calculated values are compared with the RPI observations of Figures 3 and 4 in Table 1 and Figure 6. The observed values in Table 1 and Figure 6 indicate that the peak frequency value obtained from the solution of the kappa dispersion relation at zero group velocity agree within the error bounds of the observed Qn-frequencies, whereas the calculations based upon Maxwellian distribution yields values well above the observed values. This suggests that the plasma distribution in the regions of the observations is closer to a kappa velocity distribution function with non-thermal tails, rather than to a Maxwellian distribution.

Figure 7 shows RPI data obtained from an outbound orbit when IMAGE was at a geocentric distance of about $4.9 R_E$. In this case, the plasma resonances indicated $f_{pe}/f_{ce} = (20.5 \pm 0.4)/(9.17 \pm 0.03) = 2.24 \pm 0.05$ and $f_{uh}/f_{ce} = (22.5 \pm 0.3)/(9.17 \pm 0.03) = 2.45 \pm 0.04$. The corresponding X-mode cutoff frequency is consistent with a projection to zero virtual range of the observed reflection trace. The calculated Z-mode cutoff frequency is slightly above a strong natural emission that corresponds to the calculated position of the $D1^+$ resonance and there is a sounder-stimulated resonance at $f_{uh}/2$; such features have been observed previously in the magnetosphere [Benson et al., 2003]. In addition to the main Qn resonances observed for $n = 2-4$, additional frequency components are observed. The clearest example is at 29.6 kHz on the X-antenna plasmagram in Figure 7, i.e., the short-duration sounder-stimulated resonance with what appears as a weak superimposed natural emission (observed in nearly all range bins) 1.0 kHz above the labeled Q3 resonance at 28.6 kHz. Such components to the Qn resonances have been observed previously by sounders both in the magnetosphere [see, e.g., Higel, 1978; Trotignon et al., 2001; Benson et al., 2003] and in the ionosphere [Benson, 1982]. The normalized values for what are considered to be the main Qn resonances observed in Figure 7 are presented in Table 2.

Figure 8 shows the dispersion properties of the Bernstein mode waves with $\omega > \omega_{uh}$ obtained from the numerical solution of the dispersion relation for Maxwellian and kappa distributions corresponding to the parameters of the April 6, 2002 RPI data of Figure 7. In a way similar to the previous example we found that the best value that fits the lowest and highest Qn resonances was $\kappa = 1.9$, so we fix this value for the solution of the intermediate dispersion curve. Similarly, we show only the dispersion calculations for those bands corresponding to conditions for the Qn resonances, i.e., for the bands containing the ω_{uh} and for those at higher frequencies. As before, the maximum peak of the Qn resonances for the kappa distribution, lie consistently below the value obtained from a Maxwellian distribution. These calculated values are compared with the RPI observations of Figure 7 in Table 2 and Figure 9. The values in Table 2 and Figure 9 indicate that the peak frequency values obtained from the solution of the kappa dispersion relation at zero group velocity gives better agreement with the Qn resonances than the solution based on a Maxwellian distribution, within the error bounds of the observed frequencies. The calculated value for the kappa distribution is just outside the estimated errors associated with the observed Q3 value. The calculations, however, are based on a single value for f_{pe}/f_{ce} and do not

consider the observed uncertainty in this key parameter. The better agreement obtained with the kappa distribution compared with the Maxwellian distribution, again indicates that the plasma distribution in the regions of the observations must be closer to a kappa distribution function with non-thermal tails, rather than a Maxwellian.

4. Summary & Discussion

We have investigated the perpendicular propagation of electron Bernstein waves exhibiting Qn-resonances in an isotropic non-relativistic plasma having (i) kappa and (ii) Maxwellian velocity distributions. The calculations were done using the full electromagnetic dispersion relation without employing the electrostatic assumption. The results of our calculation have been compared with the measured Qn-resonances obtained from the RPI instrument on the IMAGE satellite.

The dispersion relation for the kappa distribution shows a significant sensitivity to the shape of the distribution function, as measured by the spectral index κ in agreement with earlier results by Mace [2004]. For the isotropic case considered here, the solution of the dispersion relation depends only on three parameters, namely, the ratio of ω_{pe}/Ω_e , the ratio of the thermal velocity to the speed of light α_e/c and κ . However, over the range of frequency and wave number considered, our numerical calculations have shown that the dispersion characteristics are weakly dependent on the α_e/c ratio; thus reducing the effective parameters to two. Other models, such as the two Maxwellian component used by Belmont [1981] requires at least four parameters, and their corresponding dispersion relations are not significantly sensitivity to the shape of the distribution function.

There are some similarities between the Maxwellian and the kappa distribution resonances calculations. For example, the wave propagation is bounded by the electron cyclotron harmonics. All Qn resonances at and above the upper hybrid band have a maximum peak for both the kappa and Maxwellian distribution models. However, the maximum peak for the kappa distribution is consistently lower than that for the Maxwellian distribution. Perhaps the most important difference between the dispersion characteristics of the Qn resonances for these distributions is that the characteristics of the kappa distribution are markedly dependent on κ , (see also Mace, [2004]).

A comparison of the measured IMAGE/RPI Qn resonances with those calculated from the dispersion relations based upon both Maxwellian and kappa distributions show better agreement with the kappa distribution model. The calculated Qn resonances are also sensitive to the uncertainties in the f_{pe}/f_{ce} ratio, which may account for one estimated case where the value is just outside the estimated errors associated with the observed value for the kappa distribution; however, this issue is beyond the scope of this paper and will be addressed in a subsequent paper. In general, the good agreement with the observations suggests that the electron velocity distribution function model in the inner magnetosphere has a significant non-thermal component, which can be accurately modeled by a kappa distribution function. Furthermore, this approach can be used not only as an independent diagnostic method for determining the local electron density n_e and magnetic field strength $|\mathbf{B}|$, but also to establish a diagnostic inversion tool to

provide insights into the nature of the electron velocity distribution function in the magnetosphere.

In general, sounder excited resonances generate significant electron temperature anisotropies (i.e., $T_{\perp e} / T_{\parallel e} > 1$), near the spacecraft [James, 1983 and references therein]. At present, our calculations are for isotropic plasmas and do not consider such effects. This issue, however, will be addressed in a future publication.

5. Appendix A

Here we present a description of the electromagnetic dispersion relation for perpendicular propagating Bernstein mode waves in both kappa and Maxwellian plasmas. For the details of such calculations we refer the readers to the paper by Mace [2004] on the Bernstein modes for a kappa plasma and to [Stix, 1992; Krall and Trivelpiece, 1973; Puri et al., 1973] for the Maxwellian plasma.

The electromagnetic dispersion relation for perpendicular propagating Bernstein mode waves for a kappa distribution is given by the nontrivial solution of the determinant of a matrix tensor [Mace, 2004]

$$\Lambda_{\kappa}^{em} = \det \left| \Lambda_{\kappa}(\omega, k, \theta = 90) \right| = 0 \quad \text{where } \Lambda_{\kappa(i,j)}(\omega, \mathbf{k}) = \frac{c^2}{\omega^2} (k_i k_j - k^2 \delta_{i,j}) + \epsilon_{i,j}^{\kappa}(\omega, \mathbf{k}) \quad (\text{A.1})$$

where $\Lambda_{\kappa(i,j)}$ is a 3x3 matrix tensor and $\epsilon_{i,j}^{\kappa}$ is the dielectric tensor. The determinant of the above equation splits into two factors, one yielding the dispersion relation for ordinary modes and the other for extraordinary modes. It is the latter that will be of primary concern here, and its dispersion relation is written as [cf., Mace, 2004]

$$\epsilon_{11}^{\kappa} \left(\epsilon_{22}^{\kappa} - \frac{k^2 c^2}{\omega^2} \right) - \epsilon_{12}^{\kappa} \epsilon_{21}^{\kappa} = 0 \quad (\text{A.2})$$

where the dielectric tensor elements are defined as

$$\begin{aligned} \epsilon_{11}^{\kappa}(\omega, k) &= 1 + \sum_s \left\{ \frac{1}{k^2 \lambda_{\kappa,s}^2} - \frac{1}{2^{\kappa-1/2} \Gamma(\kappa-1/2)} \frac{\omega_{ps}^2}{\Omega_s^2 \lambda_s'} \left(\frac{\omega}{\Omega_s} \right) \csc \left(\pi \frac{\omega}{\Omega_s} \right) U_{\kappa+\frac{1}{2}, \kappa+\frac{1}{2}} \left(\frac{\omega}{\Omega_s}, \lambda_s' \right) \right\} \\ \epsilon_{12}^{\kappa}(\omega, k) &= i \sum_s \left\{ \sigma_s \frac{\omega_{ps}^2}{\Omega_s^2 \lambda_s'} \frac{1}{2^{\kappa+1/2} \Gamma(\kappa-1/2)} \csc \left(\pi \frac{\omega}{\Omega_s} \right) U_{\kappa+\frac{3}{2}, \kappa-\frac{1}{2}} \left(\frac{\omega}{\Omega_s}, \lambda_s' \right) \right\} \end{aligned} \quad (\text{A.3})$$

$$\epsilon_{21}^{\kappa}(\omega, k) = -\epsilon_{12}^{\kappa}(\omega, k)$$

$$\begin{aligned} \epsilon_{22}^{\kappa}(\omega, k) &= 1 + \sum_s \left\{ \frac{1}{k^2 \lambda_{\kappa,s}^2} - \frac{1}{2^{\kappa-1/2} \Gamma(\kappa-1/2)} \frac{\omega_{ps}^2}{\omega \Omega_s} \csc \left(\pi \frac{\omega}{\Omega_s} \right) \left[\frac{\omega^2}{\Omega_s^2 \lambda_s'} U_{\kappa+\frac{1}{2}, \kappa+\frac{1}{2}} \left(\frac{\omega}{\Omega_s}, \lambda_s' \right) \right. \right. \\ &\quad \left. \left. + 2 U_{\kappa+\frac{1}{2}, \kappa-\frac{3}{2}} \left(\frac{\omega}{\Omega_s}, \lambda_s' \right) \right] \right\} \end{aligned}$$

where σ_s is the charge state and the function $U_{\mu,v}(z, \lambda)$ is defined

$$\begin{aligned}
U_{\mu,\nu}(z, \lambda) = & 2^{\mu-1} \pi^{3/2} \csc(\pi\nu) \left[\frac{\Gamma((\mu-\nu+1)/2) \Gamma((\mu-\nu+2)/2)}{\Gamma(1-\nu) \Gamma((\mu-\nu+2)/2+z) \Gamma((\mu-\nu+2)/2-z)} \right. \\
& \times (2\lambda)^{\mu/2-\nu/2} {}_2F_3 \left[\begin{matrix} \frac{\mu}{2} - \frac{\nu}{2} + \frac{1}{2}, \frac{\mu}{2} - \frac{\nu}{2} + 1; 1-\nu, \frac{\mu}{2} - \frac{\nu}{2} + 1+z, \frac{\mu}{2} - \frac{\nu}{2} + 1-z; 2\lambda \end{matrix} \right] \\
& - \frac{\Gamma((\mu+\nu+1)/2) \Gamma((\mu+\nu+2)/2)}{\Gamma(1+\nu) \Gamma((\mu+\nu+2)/2+z) \Gamma((\mu+\nu+2)/2-z)} \\
& \left. \times (2\lambda)^{\mu/2+\nu/2} {}_2F_3 \left[\begin{matrix} \frac{\mu}{2} + \frac{\nu}{2} + \frac{1}{2}, \frac{\mu}{2} + \frac{\nu}{2} + 1; 1+\nu, \frac{\mu}{2} + \frac{\nu}{2} + 1+z, \frac{\mu}{2} + \frac{\nu}{2} + 1-z; 2\lambda \end{matrix} \right] \right] \quad (\text{A.4})
\end{aligned}$$

and $\lambda_{\kappa,s}$ and λ_s' are defined as

$$\lambda_{\kappa,s} = \left[\frac{(\kappa-3/2)}{(\kappa-1/2)} \frac{\alpha_s^2}{\omega_{ps}^2} \right]^{1/2} \quad \text{and} \quad \lambda_s' = (\kappa-3/2) k^2 \alpha_s^2 / \Omega_s^2. \quad (\text{A.5})$$

Similarly, the electromagnetic dispersion relation for perpendicular propagating Bernstein mode waves for a Maxwellian distribution is given by the nontrivial solution of the determinant of a matrix tensor [Stix, 1992; Krall and Trivelpiece, 1973; Puri et al., 1973]

$$\Lambda^{em} = \det[\Lambda(\omega, k, \theta = 90)] = 0 \quad \text{where} \quad \Lambda_{i,j}(\omega, \mathbf{k}) = \frac{c^2}{\omega^2} (k_i k_j - k^2 \delta_{i,j}) + \epsilon_{i,j}(\omega, \mathbf{k}) \quad (\text{A.6})$$

where $\Lambda_{i,j}$ is a 3x3 matrix tensor and $\epsilon_{i,j}$ is the dielectric tensor. The determinant of the above equation splits into two factors, one yielding the dispersion relation for ordinary modes and the other for extraordinary modes. Here we are only concerned with the extraordinary mode.

$$\epsilon_{11} \left(\epsilon_{22} - \frac{k^2 c^2}{\omega^2} \right) - \epsilon_{12} \epsilon_{21} = 0 \quad (\text{A.7})$$

where the dielectric tensor elements are defined as

$$\begin{aligned}
\epsilon_{11}(k, \omega) &= 1 + \sum_s \sum_{n=-\infty}^{n=+\infty} \frac{\omega_{ps}^2}{\omega(n\Omega_s - \omega)} \frac{n^2 \Lambda_n(\lambda_s)}{\lambda_s} \\
\epsilon_{12}(k, \omega) &= i \sum_s \sum_{n=-\infty}^{n=+\infty} \frac{\sigma_s \omega_{ps}^2}{\omega(n\Omega_s - \omega)} (n \Lambda_n'(\lambda_s)) \\
\epsilon_{21}(k, \omega) &= -\epsilon_{12}(k, \omega) \\
\epsilon_{22}(k, \omega) &= 1 + \sum_s \sum_{n=-\infty}^{n=+\infty} \frac{\omega_{ps}^2}{\omega(n\Omega_s - \omega)} \left(\frac{n^2 \Lambda_n(\lambda_s)}{\lambda_s} - \lambda_s \Lambda_n'(\lambda_s) \right)
\end{aligned} \quad (\text{A.8})$$

where we defined $\Lambda_n(\lambda_s) = e^{-\lambda_s} I_n(\lambda_s)$, I_n is the modified Bessel function and Λ'_n is the derivative with respect to λ_s . Comparing the square of the normalized wave vector for a kappa (λ'_s) and a Maxwellian plasma (λ_s) we have

$$\lambda'_s = (\kappa - 3/2) \lambda_s = (\kappa - 3/2) k^2 \rho_s^2. \quad (\text{A.9})$$

Acknowledgements. We are grateful to B. W. Reinish, Principal Investigator of the RPI on IMAGE for providing access to the data, J. L. Green for his helpful comments on the manuscript, and to V. Osherovich for the many discussions and his insightful comments.

References

- Abraham-Shrauner, B., and W. C. Feldman, Electromagnetic ion-cyclotron wave growth rates and their variation with velocity distribution shape, *J. Plasma Phys.*, **17**, 123-131, 1977a.
- Abraham-Shrauner, B., and W. C. Feldman, Whistler heat flux instability in the solar wind with bi-Lorentzian velocity distribution function, *J. Geophys. Res.*, **82**, 1889-1892, 1977b.
- Belmont, G., Characteristics frequencies of a non-Maxwellian plasma: A method for localizing the exact frequencies of magnetospheric intense waves near f_{pe} , *Planet. Space Sci.*, **29**, 1251-1266, 1981.
- Benson, R. F., Stimulated plasma waves in the ionosphere, *Radio Sci.*, **12**, 861-878, 1977.
- Benson, R.F., Stimulated plasma instability and nonlinear phenomena in the ionosphere, *Radio Sci.*, **17**, 1637-1659, 1982.
- Benson, R.F., and V.A. Osherovich, High order stimulated ionospheric diffuse plasma resonances - significance to magnetospheric emissions, *J. Geophys. Res.*, **97**, 19,413-19,419, 1992.
- Benson, R. F., V. A. Osherovich, J. Fainberg, A. F.-Viñas, and D. R. Ruppert, An interpretation of banded magnetospheric radio emissions, *J. Geophys. Res.*, **106**, 13179-13190, 2001.
- Benson, R. F., V. A. Osherovich, J. Fainberg, and B. W. Reinisch, Classification of IMAGE/RPI-stimulated plasma resonances for the accurate determination of magnetospheric electron density and magnetic field values, *J. Geophys. Res.*, **108**(A5), 1207, 2003.
- Christiansen, P., P. Gough, G. Martelli, J-J. Block, N. Cornilleau, J. Etcheto, R. Gendrin, D. Jones, C. Béghin and P. Décréau, Geos I: Identification of natural magnetospheric emissions, *Nature*, **272**, 682-686, 1978.
- Higel, B., Small scale structure of magnetospheric electron density through on-line tracking of plasma resonances, *Space Sci. Rev.*, **22**, 611-631, 1978.
- James, H.G., Souder-accelerated particles observed on ISIS, *J. Geophys. Res.*, **88**, 4027-4040, 1983.
- Kamimura, T., T. Wagner and J. M. Dawson, Simulation study of Bernstein modes, *Phys. Fluids*, **21**, 1151-1167, 1978.
- Krall, N. A. and A. W. Trivelpiece, Principles of Plasma Physics, McGraw-Hill Co., New York, pg 407-413, 1973.
- Kurth, W.S., Comparative observations of plasma waves at the outer planets, *Adv. Space Res.*, **12** (8), (8)83-(8)90, 1992.

- Leubner, M. P., Fundamental issues on kappa-distributions in space plasmas and interplanetary proton distributions, *Phys. Plasmas*, 11, 1308-1316, 2004.
- Mace, R. L., A dielectric tensor for a uniform magnetoplasma with a generalized Lorentzian distribution, *J. Plasma Phys.*, 55, 415-429, 1996.
- Mace, R. L., A Gordeyev integral for electrostatic waves in a magnetized plasma with a kappa velocity distribution, *Phys. Plasmas*, 10, 2181--2193, 2003.
- Mace, R. L., Generalized electron Bernstein modes in a plasma with a kappa velocity distribution, *Phys. Plasmas*, 11, 507-522, 2004.
- Meyer-Vernet, N. S., On natural noises detected by antennas in plasmas, *J. Geophys. Res.*, 84, 5373-5377, 1979.
- Muldrew, D. B., Electron resonances observed with topside sounders, *Radio Sci.*, 7, 779-789, 1972a.
- Muldrew, D.B., Electrostatic resonances associated with the maximum frequencies of cyclotron-harmonic waves, *J. Geophys. Res.*, 77, 1794-1801, 1972b.
- Osherovich, V.A., R.F. Benson, J. Fainberg, R.G. Stone, and R.J. MacDowall, Sounder stimulated Dn Resonances in Jupiter's Io plasma torus, *J. Geophys. Res.*, 98 (E10), 18751-18756, 1993.
- Oya, H., Conversion of electrostatic plasma waves into electromagnetic waves: numerical calculation of the dispersion relation for all wavelengths, *Radio Sci.*, 12, 1131-1141, 1971.
- Puri, S., F. Leuterer, and M. Tutter, Dispersion curves for the generalized Bernstein modes, *J. Plasma Phys.*, 9, 89-100, 1973.
- Reinisch, B.W., D.M. Haines, K. Bibl, G. Cheney, I.A. Gulkin, X. Huang, S.H. Myers, G.S. Sales, R.F. Benson, S.F. Fung, J.L. Green, W.W.L. Taylor, J.-L. Bougeret, R. Manning, N. Meyer-Vernet, M. Moncuquet, D.L. Carpenter, D.L. Gallagher, and P. Reiff, The radio plasma imager investigation on the IMAGE spacecraft, *Space Sci. Rev.*, 91 (2), 319-359, 2000.
- Sentman, D. D., Thermal fluctuations and the diffuse electrostatic emissions, *J. Geophys. Res.*, 87, 1455-1472, 1982.
- Stix, T. H., *Waves In Plasmas*, American Institute of Physics (AIP), New York, pg. 277-300, 1992.

Trotignon, J.G., P.M.E. Decreau, J.L. Rauch, P. Canu, and et al., How to determine the thermal electron density and the magnetic field strength from the Cluster/Whisper observations around the earth, *Ann. Geophysicae*, 19, 1711-1720, 2001.

Tsallis, C., Possible generalization of Boltzmann-Gibbs statistics, *J. Stat. Phys.*, 52, 479, 1988.

Tsallis, C., and Brigatti E., Nonextensive statistical mechanics: A brief introduction, *Continuum Mech. Thermodyn.*, 16, 223, 2004.

Tsallis, C., Nonextensive statistical mechanics: construction and physical interpretation in *Nonextensive Entropy-Interdisciplinary Applications*, ed. By M. Gell-Mann and C. Tsallis, pp. 1-54, Oxford University Press, New York, 2004.

Table 1. Observed and calculated normalized Qn corresponding to the IMAGE/RPI data for Figures 3 and 4 (April 8, 2002, 1508:25 UT). These calculations are based on a kappa distribution function with $\kappa = 2.1$ and an electron temperature $T_e = 51$ eV. The values of $f_{uh}/f_{ce} = 5.67 \pm 0.07$, $f_{pe}/f_{ce} = 5.58 \pm 0.07$, and $f_{ce} = 4.73 \pm 0.08$ kHz were used.

n	Observed (f_{Qn}/f_{ce})	Std. Dev. ($\pm\sigma_n$)	Kappa Calculated (f_{Qn}/f_{ce})	Kappa $k\rho_e$	Maxwellian Calculated (f_{Qn}/f_{ce})	Maxwellian $k\rho_e$
5	5.81	0.05	5.767	0.977	5.930	1.517
6	6.38	0.05	6.430	2.810	6.619	2.908
7	7.23	0.05	7.280	4.470	7.420	4.016
8	8.14	0.06	8.199	5.560	8.299	5.042
9	9.07	0.06	9.150	6.742	9.224	6.022

Table 2. Same as Table 1 but corresponding to the IMAGE/RPI data for Figure 7 (April 6, 2002, 0530:57 UT) with $\kappa = 1.9$ and an electron temperature $T_e = 51$ eV, $f_{uh}/f_{ce} = 2.45 \pm 0.05$ ($f_{pe}/f_{ce} = 2.24 \pm 0.05$).

n	Observed (f_{Qn}/f_{ce})	Measured Std. Dev. ($\pm\sigma_n$)	Kappa Calculated (f_{Qn}/f_{ce})	Kappa $k\rho_e$	Maxwellian Calculated (f_{Qn}/f_{ce})	Maxwellian $k\rho_e$
2	2.55	0.02	2.54	0.611	2.60	0.795
3	3.12	0.02	3.21	2.153	3.28	1.928
4	4.07	0.03	4.11	3.438	4.16	2.881

Figure Captions

Figure 1. Kappa distributions, in arbitrary normalized units, for different κ values ($\kappa = \infty$ corresponds to a Maxwellian velocity distribution).

Figure 2. Dispersion curves for kappa velocity distribution (dashed lines) and Maxwellian distribution (solid lines) for plasma parameters $f_{uh}/f_{ce} = 4.5$ ($f_{pe}/f_{ce} = 4.39$), $\alpha_e/c = 0.01$ ($T_e = 51\text{eV}$), and $\kappa = 2$ as obtained from the electromagnetic dispersion relation in A.2 and A.7.

Figure 3. (top) RPI plasmagram recorded at 1508:25 UT on 8 April 2002 displaying the virtual range of the color-coded signal strength received on the x antenna as a function of sounding frequency in 134 steps of 0.3 kHz (the receiver bandwidth) from 6 to 46 kHz. The scaled values for the plasma resonances identified as occurring at nf_{ce} , f_{pe} , f_{uh} , and f_{Qn} , are designated at the top by n, p, u, and Qn, respectively. The propagation cutoff frequency at the satellite for the X-mode echo, as calculated from the resonance-determined f_{ce} and f_{pe} values, is designated at the top by an x. (bottom) Portion of the IMAGE orbit (red trace) projected in the x-z plane with $L = 4$ and $L = 6.5$ dipole field lines included.

Figure 4. (top) Expanded version (26 to 46 kHz) of the 1508:25 UT, 8 April 2002 RPI plasmagram of Figure 3 highlighting the Qn resonances. (middle and bottom). Same for the y and z antennas, respectively.

Figure 5. Numerical solution of the electromagnetic dispersion relation for kappa velocity distribution (dashed lines) and Maxwellian distribution (solid lines) for conditions appropriate to the RPI data of Figures 3 and 4, i.e., $f_{uh}/f_{ce} = 5.666$ ($f_{pe}/f_{ce} = 5.577$), $\alpha_e/c = 0.01$ ($T_e = 51\text{eV}$), and $\kappa = 2.1$.

Figure 6. Comparison of the Qn resonance calculations based upon a kappa velocity distribution (dashed line) and Maxwellian distributions (solid line) with the RPI observed Qn frequencies (open circles).

Figure 7. Same as Figure 3 except for the x, y and z antenna RPI plasmagrams recorded at 0520:57 UT on 6 April 2002. In this case, besides the labeled features in Figure 3, a resonance identified as $f_{uh}/2$ is labeled as u/2 and the propagation cutoff frequency at the satellite for the Z-mode echo, as calculated from the resonance-determined f_{ce} and f_{pe} values, is labeled as z.

Figure 8. Same as in Figure 5 but for conditions appropriate to the RPI data of Figure 7, i.e., $f_{uh}/f_{ce} = 2.454$ ($f_{pe}/f_{ce} = 2.241$), $\alpha_e/c = 0.01$ ($T_e = 51\text{eV}$), and $\kappa = 1.9$.

Figure 9. Similar to Figure 6 but for conditions appropriate to the RPI data in Figure 7.

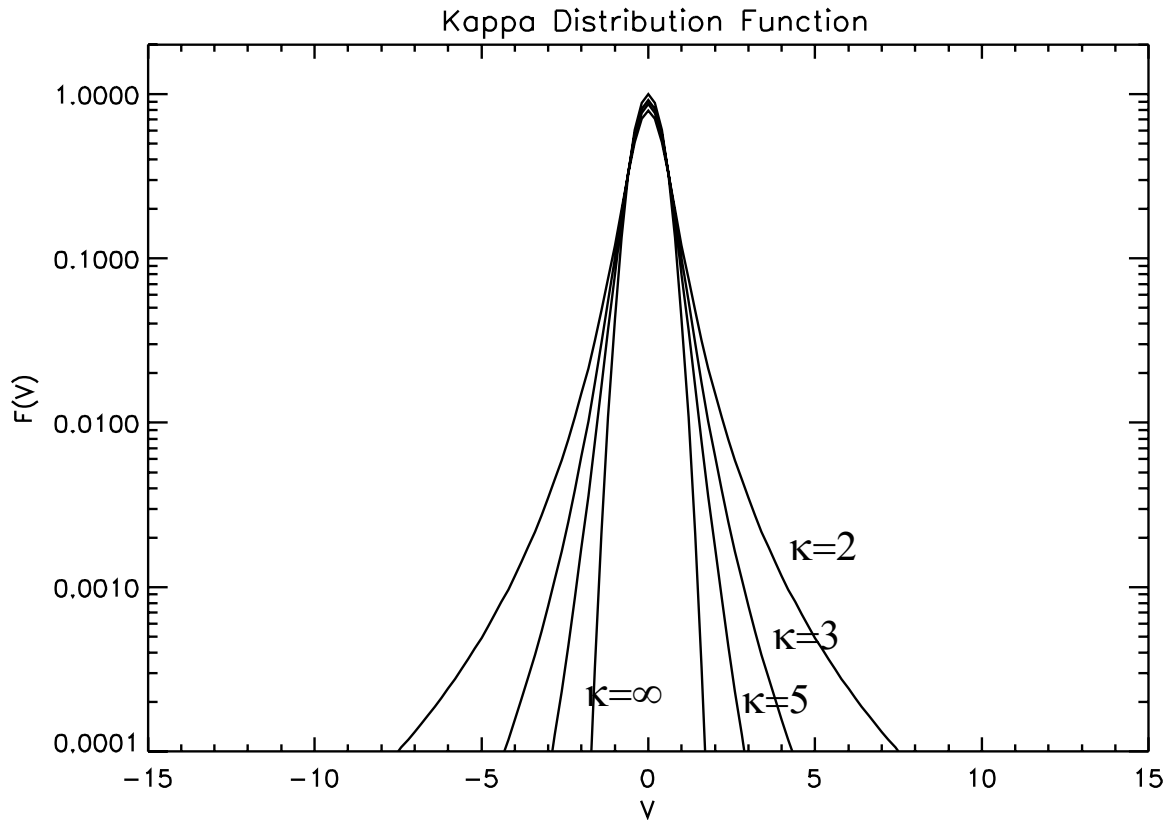


Figure 1. Kappa distributions, in arbitrary normalized units, for different κ values ($\kappa = \infty$ corresponds to a Maxwellian velocity distribution).

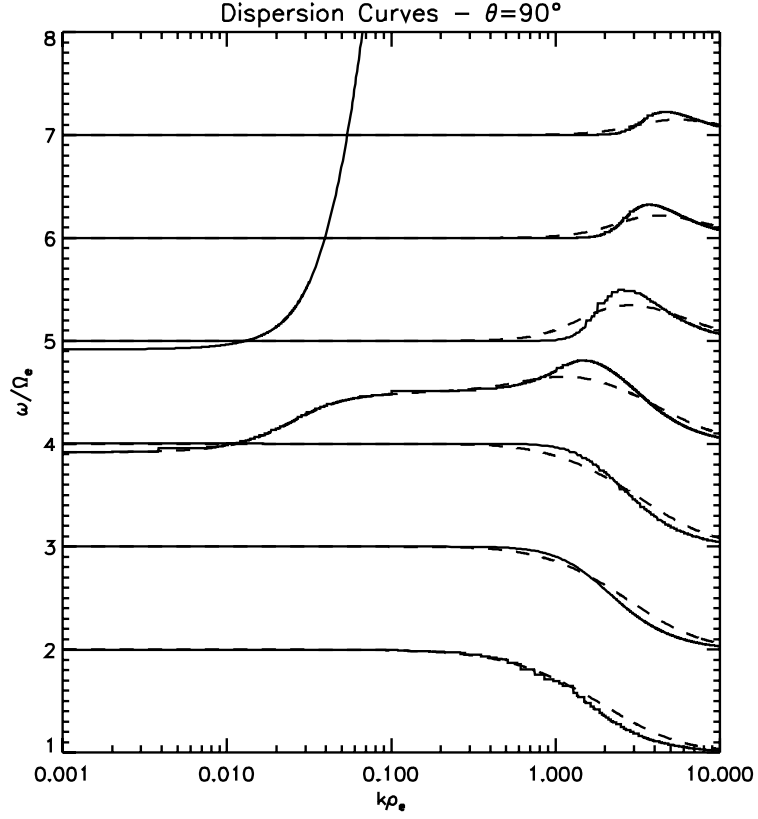


Figure 2. Dispersion curves for kappa velocity distribution (dashed lines) and Maxwellian distribution (solid lines) for plasma parameters $f_{uh}/f_{ce} = 4.5$ ($f_{pe}/f_{ce} = 4.39$), $\alpha_e/c = 0.01$ ($T_e = 51\text{eV}$), and $\kappa = 2$ as obtained from the electromagnetic dispersion relation in A.2 and A.7.

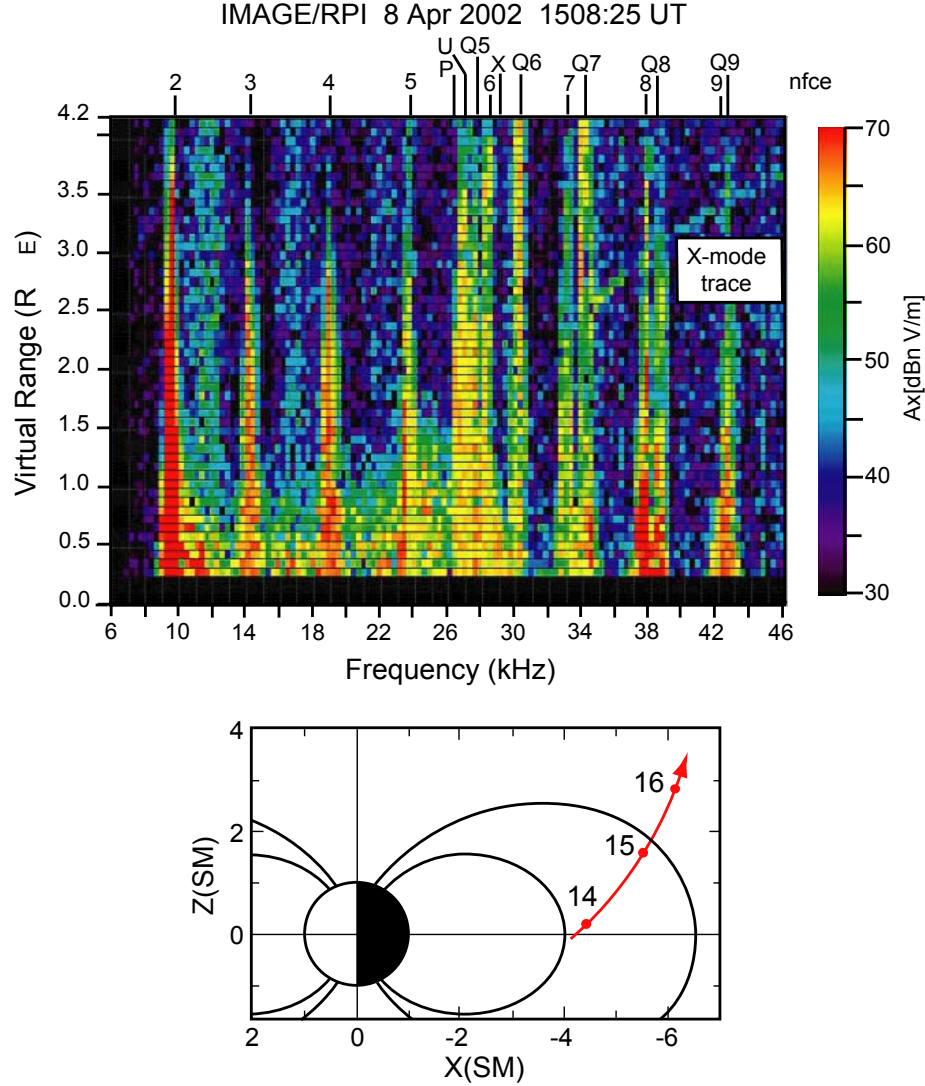


Figure 3. (top) RPI plasmagram recorded at 1508:25 UT on 8 April 2002 displaying the virtual range of the color-coded signal strength received on the x antenna as a function of sounding frequency in 134 steps of 0.3 kHz (the receiver bandwidth) from 6 to 46 kHz. The scaled values for the plasma resonances identified as occurring at nf_{ce} , f_{pe} , f_{uh} , and f_{Qn} , are designated at the top by n, p, u, and Qn , respectively. The propagation cutoff frequency at the satellite for the X-mode echo, as calculated from the resonance-determined f_{ce} and f_{pe} values, is designated at the top by an x. (bottom) Portion of the IMAGE orbit (red trace) projected in the x-z plane with $L = 4$ and $L = 6.5$ dipole field lines included.

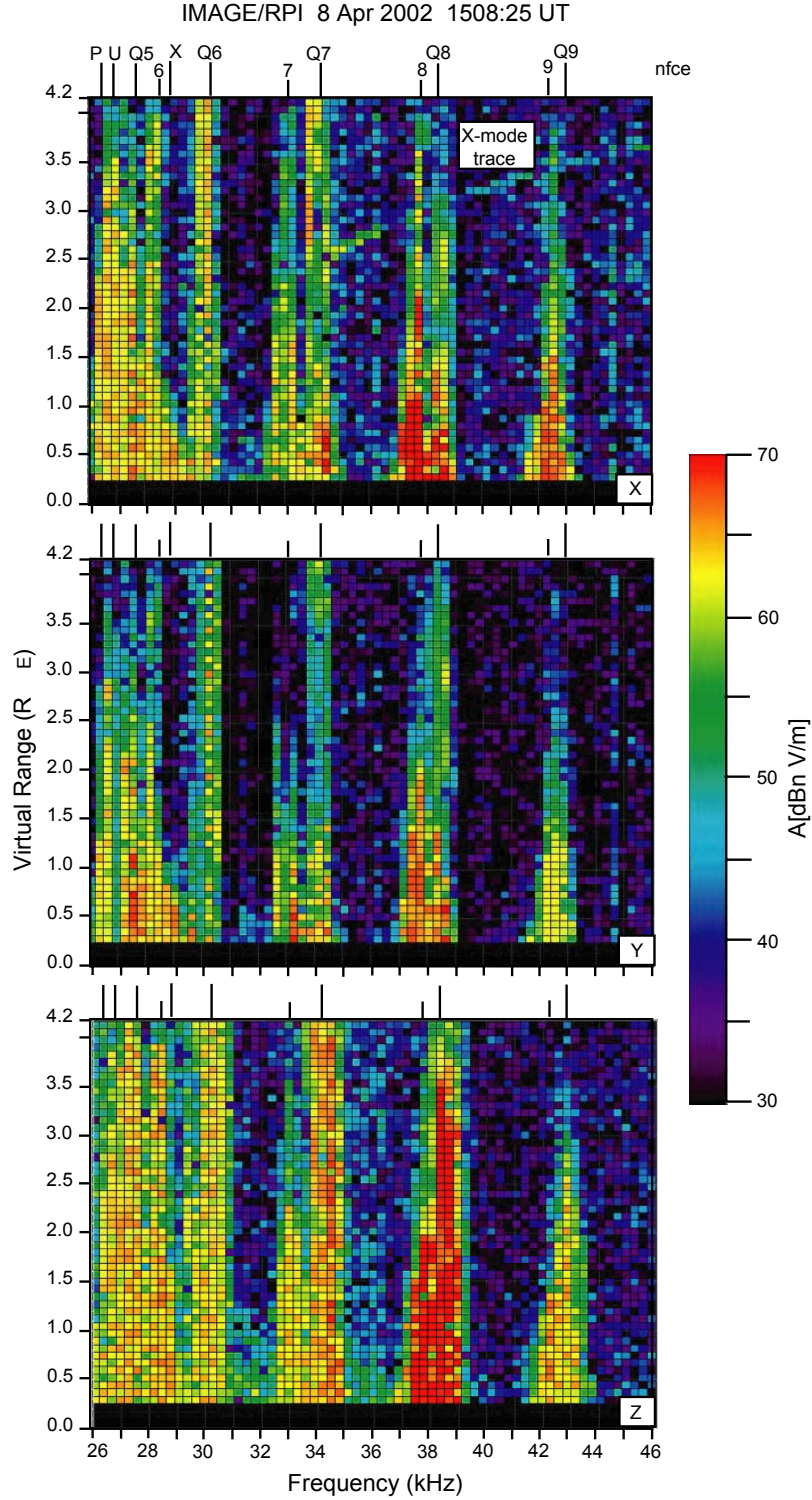


Figure 4. (top) Expanded version (26 to 46 kHz) of the 1508:25 UT, 8 April 2002 RPI plasmaGRAM of Figure 3 highlighting the Qn resonances. (middle and bottom). Same for the y and z antennas, respectively.

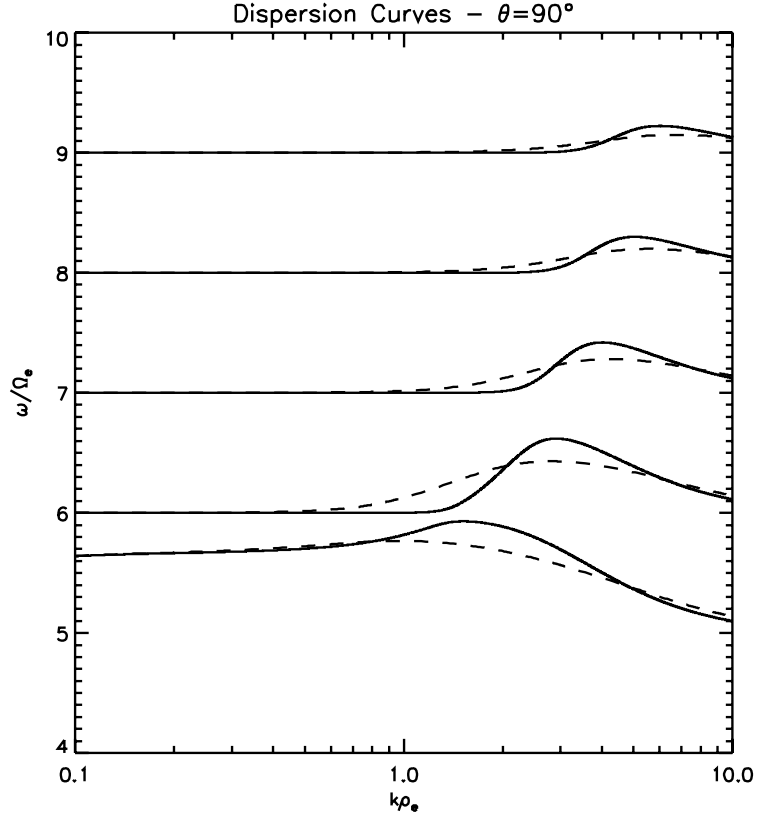


Figure 5. Numerical solution of the electromagnetic dispersion relation for kappa velocity distribution (dashed lines) and Maxwellian distribution (solid lines) for conditions appropriate to the RPI data of Figures 3 and 4, i.e., $f_{uh}/f_{ce} = 5.666$ ($f_{pe}/f_{ce} = 5.577$), $\alpha_e/c = 0.01$ ($T_e = 51\text{eV}$), and $\kappa = 2.1$.

IMAGE/RPI Qn Resonances 8 April 2002 1508:25 UT
 $f_{pe}/f_{ce} = 5.58$ $\text{Kappa} = 2.1$

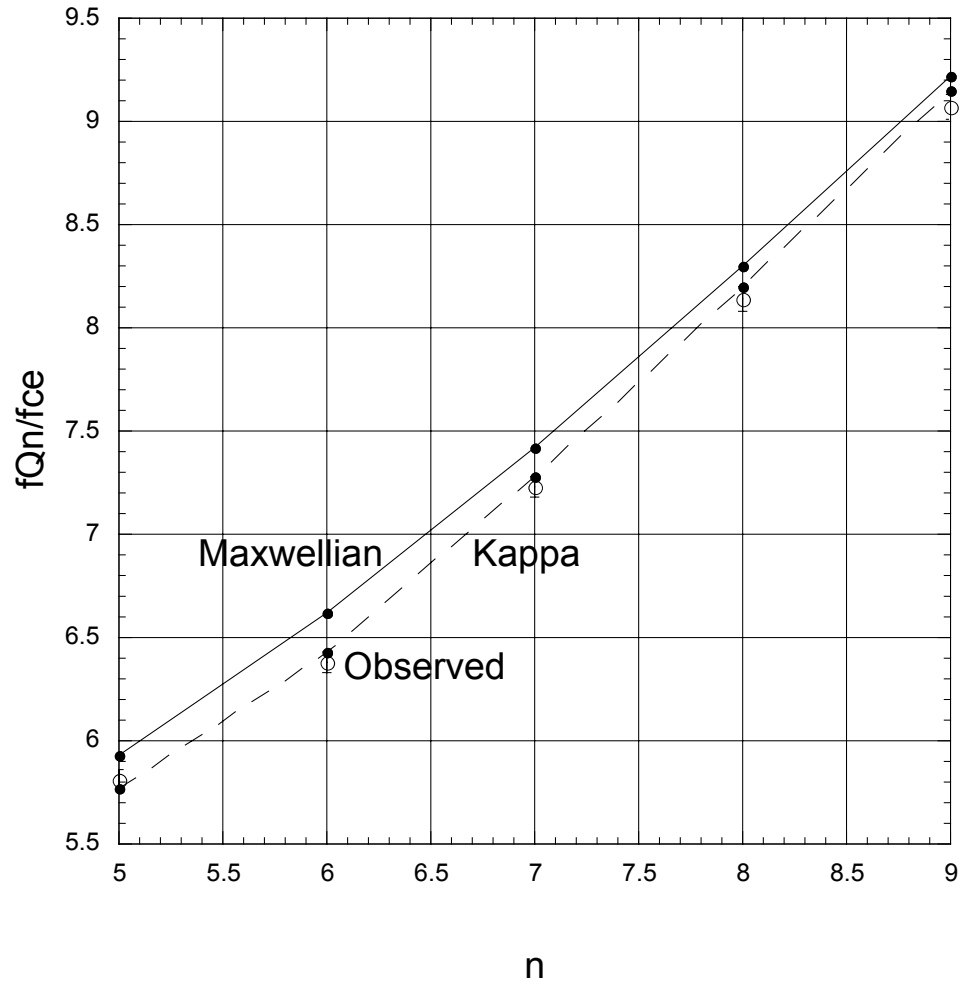


Figure 6. Comparison of the Qn resonance calculations based upon a kappa velocity distribution (dashed line) and Maxwellian distributions (solid line) with the RPI observed Qn frequencies (open circles).

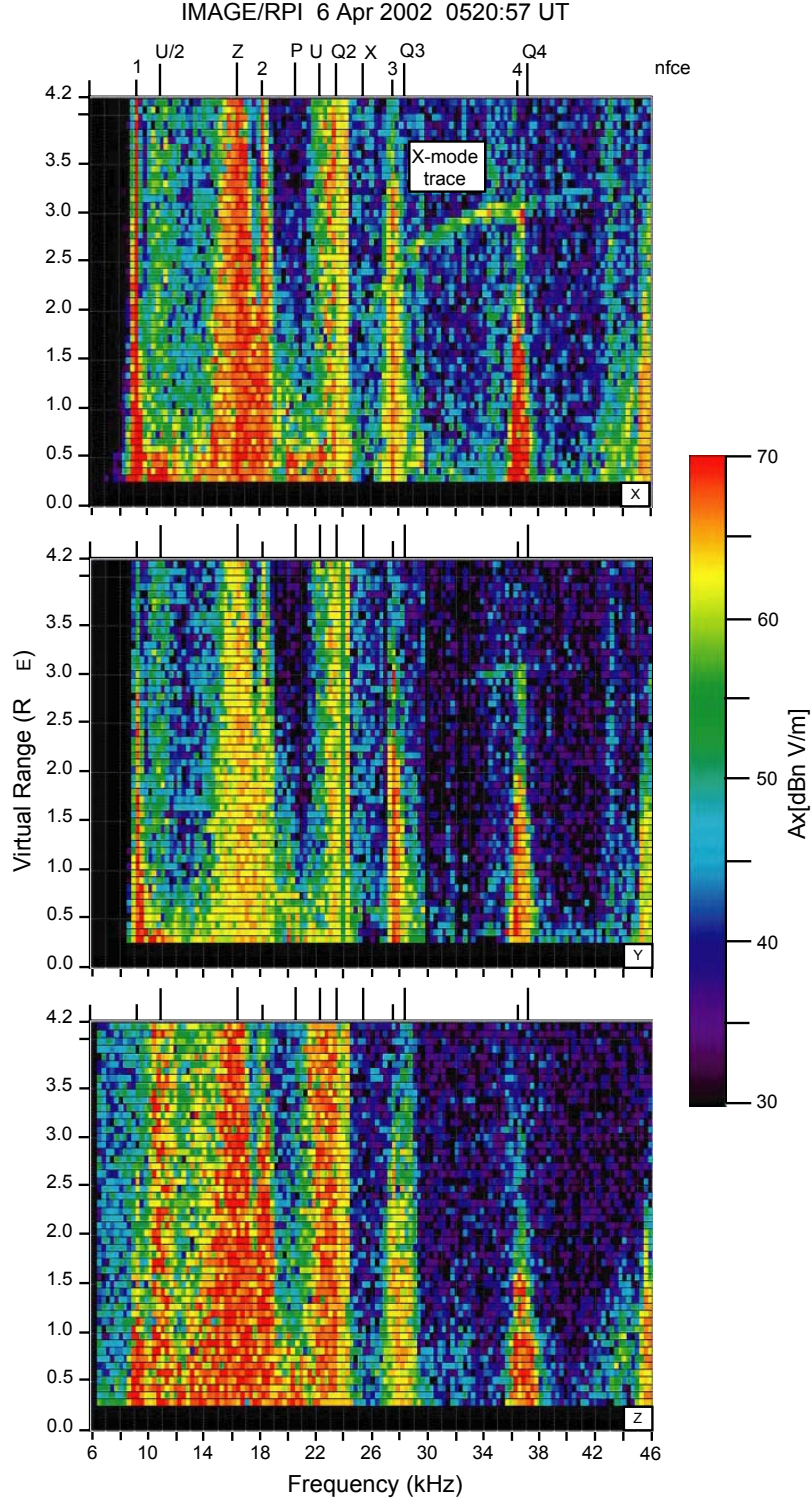


Figure 7. Same as Figure 3 except for the x, y and z antenna RPI plasmagrams recorded at 0520:57 UT on 6 April 2002. In this case, besides the labeled features in Figure 3, a resonance identified as $f_{uh}/2$ is labeled as u/2 and the propagation cutoff frequency at the satellite for the Z-mode echo, as calculated from the resonance-determined f_{ce} and f_{pe} values, is labeled as z.

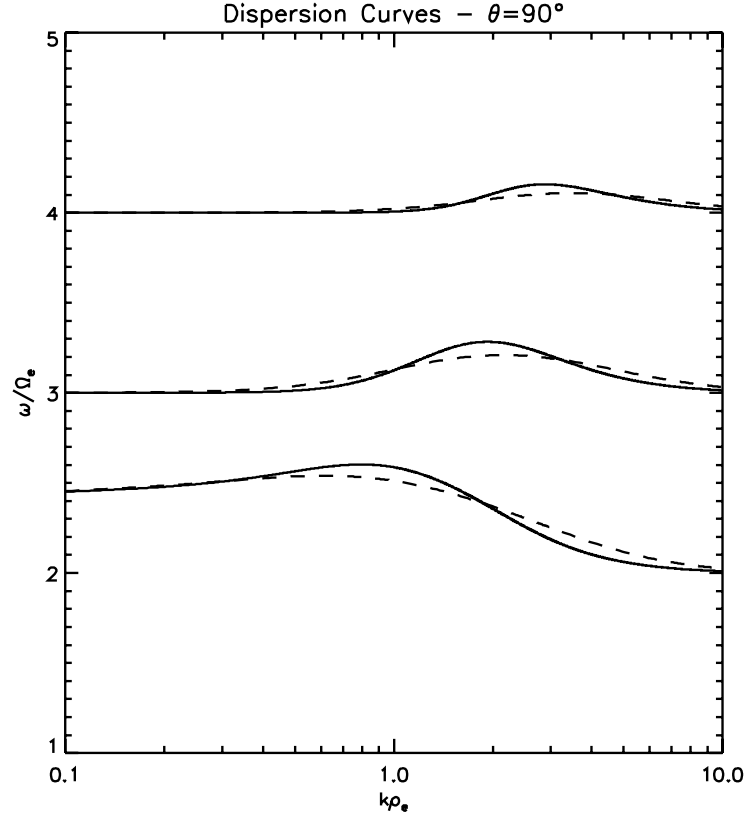


Figure 8. Same as in Figure 5 but for conditions appropriate to the RPI data of Figure 7, i.e., $f_{uh}/f_{ce} = 2.454$ ($f_{pe}/f_{ce} = 2.241$), $\alpha_e/c = 0.01$ ($T_e = 51\text{eV}$), and $\kappa = 1.9$.

IMAGE/RPI Qn Resonances 6 April 2002 0520:57 UT
 $f_{pe}/f_{ce} = 2.24$ $\text{Kappa} = 1.9$

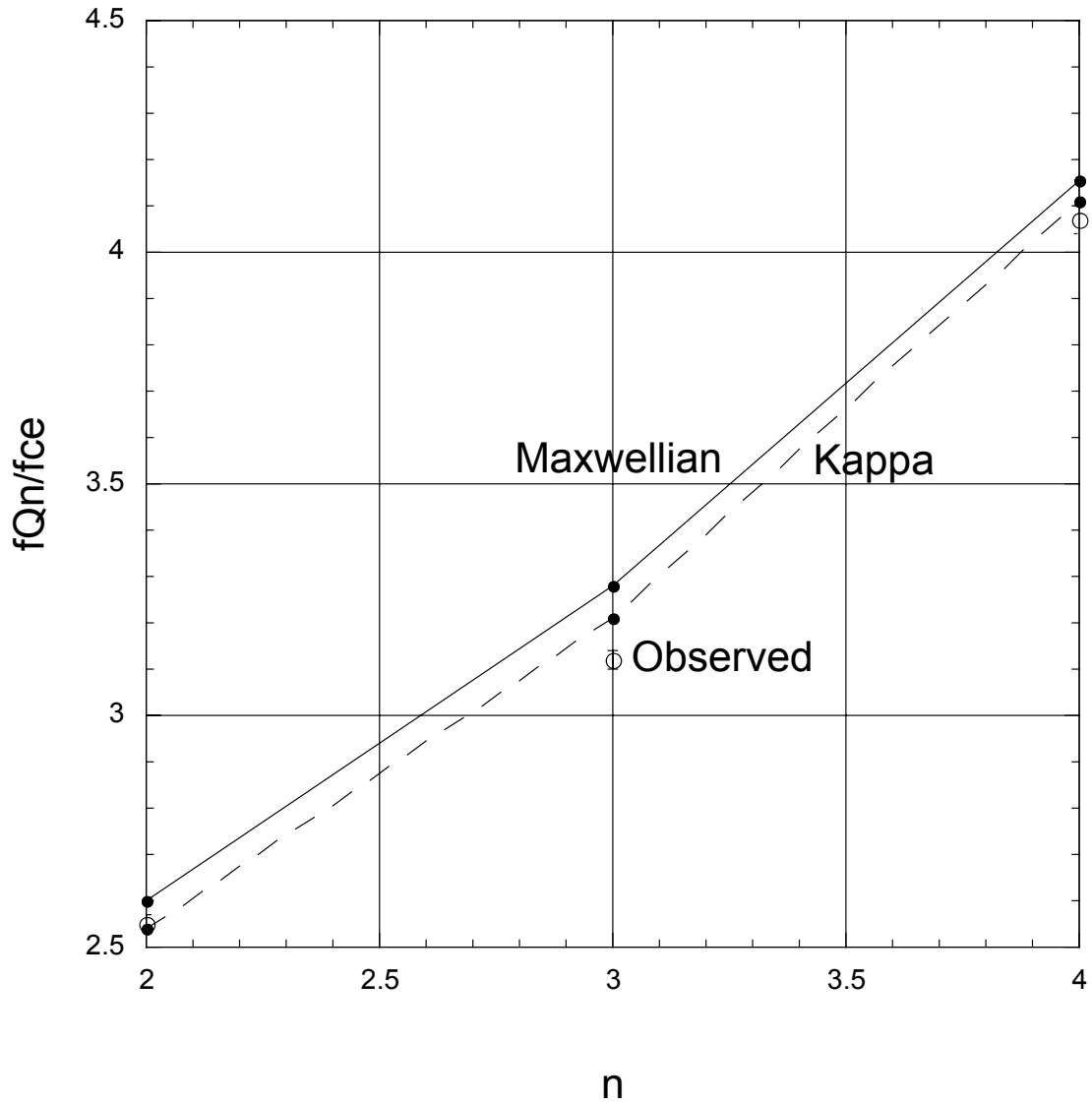


Figure 9. Similar to Figure 6 but for conditions appropriate to the RPI data in Figure 7.